

The detection of radio emission from known X-ray flaring star EXO 040830–7134.7

L. N. Driessen,^{1*} D. R. A. Williams,¹ I. McDonald,^{1,2} B. W. Stappers,¹
D. A. H. Buckley,^{3,4} R. P. Fender,^{5,6} P. A. Woudt,^{4,6}

¹*Jodrell Bank Centre for Astrophysics, Department of Physics and Astronomy, The University of Manchester, Manchester, M13 9PL, UK*

²*School of Physics and Astronomy, Open University, Walton Hall, Milton Keynes, MK7 6AA, UK*

³*South African Astronomical Observatory, PO Box 9, Observatory 7935, South Africa*

⁴*Department of Astronomy, University of Cape Town, Private Bag X3, Rondebosch 7701, South Africa*

⁵*Department of Physics, Astrophysics, University of Oxford, Denys Wilkinson Building, Keble Road, Oxford OX1 3RH, UK*

⁶*Inter-University Institute for Data Intensive Astronomy, Department of Astronomy, University of Cape Town, Private Bag X3, Rondebosch 7701, South Africa*

Accepted 2021 November 25. Received 2021 November 25; in original form 2021 August 25

ABSTRACT

We report the detection of radio emission from the known X-ray flaring star EXO 040830–7134.7 during MeerKAT observations of the nearby cataclysmic variable VW Hydri. We have three epochs of MeerKAT observations, where the star is not detected in the first epoch, is detected in the second epoch, and is marginally detected in the third epoch. We cannot distinguish whether the detection is quiescent emission or a transient radio burst. If we assume the radio detection is quiescent emission the source lies somewhat to the right of the Güdel–Benz relation; however, if we assume the upper-limit on the radio non-detection is indicative of the quiescent emission then the source lies directly on the relation. Both cases are broadly consistent with the relation. We use archival spectral energy distribution data and new SALT high-resolution spectroscopy to confirm that EXO 040830–7134.7 is a chromospherically active M-dwarf with a temperature of 4000 ± 200 K of spectral type M0V. We use ASAS, ASAS-SN and TESS optical photometry to derive an improved rotational period of 5.18 ± 0.04 days. This is the first radio detection of the source, and the first MeerKAT detection of an M-dwarf.

Key words: stars: flare – stars: variables: general – radio continuum: stars

1 INTRODUCTION

Observing stellar radio variability reveals information about particle acceleration and magnetic fields in stellar atmospheres (e.g. Villadsen & Hallinan 2019; Matthews 2019) and is also important for determining the habitability of planets orbiting active stars (e.g. Villadsen 2017). It has been hypothesised that the quiescent radio and X-ray emission from active stars is due to many small flares (e.g. Forbrich et al. 2011; Villadsen 2017). Many cool M-dwarfs tend to be active and are known to host low-mass planets (Dressing & Charbonneau 2015; Hardegree-Ullman et al. 2019). The population of known active stars and stellar binaries include T-Tauri stars, RS Canum Venaticorum (RS CVn) binaries, Algol binaries, and Cataclysmic Variable (CV) binaries. Therefore, it is essential to improve our understanding of the radio nature and variability of main-sequence stars, and thereby the impact of stellar flares on orbiting planets.

An empirical relation that is often used to determine whether a star is a member of the population of incoherent radio stellar sources is the Güdel–Benz relation. This relation describes a

correlation between the radio and X-ray luminosities of stellar radio sources and is given by $L_X/L_R \approx 10^{15.5}$ where L_R and L_X are the quiescent radio specific and X-ray luminosities respectively (Guedel & Benz 1993). This relation extends across many magnitudes of X-ray and radio luminosities and applies to solar flares, RS CVn binaries, and BY Draconis-type binaries, as well as active M- and K-type stars. A similar relation exists for Algol systems, FK Com stars, and post T Tauri stars (Benz & Guedel 1994). The Güdel–Benz relation suggests that the mechanism that heats the coronae of active stars is the same mechanism that accelerates non-thermal electrons. The model commonly used to explain this is that magnetic reconnection events in the corona accelerates electrons to produce gyrosynchrotron emission. These non-thermal electrons lose energy in the chromosphere, heating the corona and results in thermal X-ray emission (Benz & Guedel 1994). This means that radio observations of gyrosynchrotron emission from active stars probe the conditions in the stellar corona (e.g. Bastian 1990), that cannot be probed at other wavelengths. The gyrosynchrotron emission is detected as incoherent radio emission with low circular polarisation fractions and low brightness temperature ($T_b \lesssim 10^{12}$ K). Stars are also observed to emit coherent radio emission, which is caused by a different emission mechanism,

* E-mail: Laura@Driessen.net.au (LND)

either plasma or electron-cyclotron maser (ECM) emission (Dulk 1985). Coherent radio emission has $T_b \gtrsim 10^{12}$ K and a high circular polarisation fraction. Coherent radio emission also violates the Güdel-Benz relation, as recently demonstrated by Callingham et al. (2021) using Low-Frequency Array ($\lesssim 200$ MHz) detections of coherent radio emission from a population of M-dwarfs. They found that the radio luminosities of their sources did not correlate with the X-ray luminosity, which suggests that the radio emission is not linked to chromospheric activity. This is particularly interesting as low-frequency, coherent emission from stars could be caused by ECM emission, where there is a magnetic connection between the M-dwarf and an orbiting planet similar to the Jupiter-Io system (Vedantham et al. 2020; Callingham et al. 2021). Auroral activity on the M-dwarf UV Ceti caused by ECM emission has also been detected at 888 MHz using the Australian Square Kilometer Array Pathfinder (ASKAP¹; Zic et al. 2020; Hotan et al. 2021). These results show that we still have more to learn and discover using radio observations of stellar sources.

EXO 040830–7134.7 (hereafter EXO 0408) was first discovered serendipitously by van der Woerd et al. (1989) during the European Space Agency’s X-ray Observatory (*EXOSAT*; White & Peacock 1988) observations of the CV system VW Hydri (VW Hyi). VW Hyi was observed 30 times by *EXOSAT* between 1983 and 1985, for a total of 84.1 hours. In 29 of the 30 observations, EXO 0408 was observed as a weak, quiescent X-ray source with a luminosity of 1.8×10^{29} erg s⁻¹ in the soft X-ray band (0.05–2.0 keV, assuming a distance of 50 kpc). It was determined by van der Woerd et al. (1989) that the X-ray source is coincident with a dMe type star of spectral type M0V, because they observe the hydrogen Balmer lines in emission. On 1984 October 11, they observed the source to flare with an X-ray flux of 1.2×10^{30} erg s⁻¹. The observation was 7,600 seconds long, and they did not observe the rise or decay of the flare. At the time, this was the longest X-ray flare observed from a dMe star. In van der Woerd et al. (1989) they hypothesise that the X-ray variability is caused by variable active regions on the surface of a rotating star.

Cutispoto et al. (1996) performed high-precision photometry on active stars discovered with *EXOSAT* using the 50 cm and 1 m ESO telescopes at La Silla, Chile. They classified EXO 0408 as an M0Ve star at a distance of 54 pc. They found some evidence of optical photometric variability with a period of 5.2 ± 0.20 days. An updated distance of 57.72 ± 0.04 pc (Bailer-Jones et al. 2021) was provided by the *Gaia* Early Data Release 3 (*Gaia* EDR3; *Gaia* Collaboration 2020a). The *Gaia* EDR3 J2016.0 position of EXO 0408 is $04^{\text{h}}08^{\text{m}}07^{\text{s}}.1371 \pm 0.''00001$ $-71^{\circ}26'59''.1953 \pm 0.''00001$ in Right Ascension and Declination respectively. To the best of our knowledge, EXO 0408 has not previously been detected in the radio.

ThunderKAT² (Fender et al. 2017) is a MeerKAT Large Survey Project (LSP) observing and investigating variable and transient radio sources such as CVs, X-ray binaries, and γ -ray bursts. ThunderKAT also performs commensal searches for variable and transient sources in the field of view (FoV) of MeerKAT observations, taking advantage of the wide ($\gtrsim 1$ square degree at 1.4 GHz) FoV and sensitivity of the telescope. The (more) Karoo Array Telescope (MeerKAT; Camilo et al. 2018) is a 64 dish radio telescope in South Africa. Each dish has an effective area of 13.5 m and the longest baseline in the array is ~ 8 km.

ThunderKAT has agreements to search commensally for variable

and transient radio sources in MeerKAT LSP observations. This includes untargeted searches, such as the search that led to the discovery of a new transient source, MKT J170456.2–482100, in MeerKAT observations of GX 339–4 (Driessen et al. 2020), and looking for possible radio variability from specific sources such as flare stars. To facilitate this, we used catalogues of flare-type objects (Lépine & Gaidos 2011; Kepler et al. 2013; Drake et al. 2009; Wenger et al. 2000; Dufour et al. 2017) to determine whether they fall into the primary beam of MeerKAT LSP observations³. Testing this method on ThunderKAT observations, revealed that EXO 0408 is within the field of view of MeerKAT in the L-band (856–1712 MHz) when it was pointed at VW Hyi.

In this paper we will present the discovery of radio emission from EXO 0408 during the MeerKAT observations of VW Hyi. In Sections 2, 3, 4, and 5 we will respectively present the radio, optical photometric, optical spectroscopic, X-ray, and Ultraviolet (UV) observations of EXO 0408. In Sections 6 and 7 we will discuss and conclude.

2 MEERKAT RADIO OBSERVATIONS

We observed the CV VW Hyi on 2018 August 05, 07 and 08 with the MeerKAT radio telescope as part of the ThunderKAT LSP during an outburst. Each observation was two hours, with ~ 1.5 hours on target per epoch with a central frequency of 1284 MHz, a bandwidth of 856 MHz, 4096 frequency channels and an integration time of 8 seconds. 61 MeerKAT antennas participated in the first two observations, while 58 antennas were available during the third observation. We interleaved ten-minute scans of the target field with two-minute scans of a bright phase calibrator: PKS 0408–65, which we also used as the flux and band-pass calibrator for all three datasets.

We reduced the data using the *Oxkat* (Heywood 2020)⁴ MeerKAT reduction scripts, which perform standard calibration and imaging procedures of MeerKAT radio data. These scripts are containerised using *singularity* (Kurtzer et al. 2017) and *strela* (Makhathini 2018). We calibrated the data using the 1GC script and CASA Version 5.6.2 (McMullin et al. 2007) software. The 1GC script averages the data to 1024 channels, performs standard phase and amplitude calibrations and applies both a priori and automated flagging of the data. We performed additional flagging (FLAG script) before imaging (2GC) of the target field using *WSClean* (Offringa et al. 2014a) and *cubicall* (Kenyon et al. 2018). We used the default *Oxkat* settings for MeerKAT data to produce the images. We performed self calibration on the target field and made the final measurement set for each observation.

We made the final images using *WSClean* (Offringa et al. 2014b), producing full time and frequency integrated images per epoch as well as images with various, shorter integration times from 16 seconds per image to half an hour per image. The root-mean-square (RMS) noise of the full integration images was 0.03 mJy beam⁻¹ in all three epochs. We also produced eight subband images per epoch with central frequencies 909, 1016, 1123, 1230, 1337, 1444, 1551, and 1658 MHz. We measured the Multi-Frequency-Synthesis (MFS) flux density of EXO 0408 and

¹ <https://www.atnf.csiro.au/projects/askap/index.html>

² The HUNt for Dynamic and Explosive Radio transients with MeerKAT

³ The code for this can be found here: <https://doi.org/10.5281/zenodo.4515114>

⁴ The analysis scripts can be found at <https://github.com/IanHeywood/oxkat>

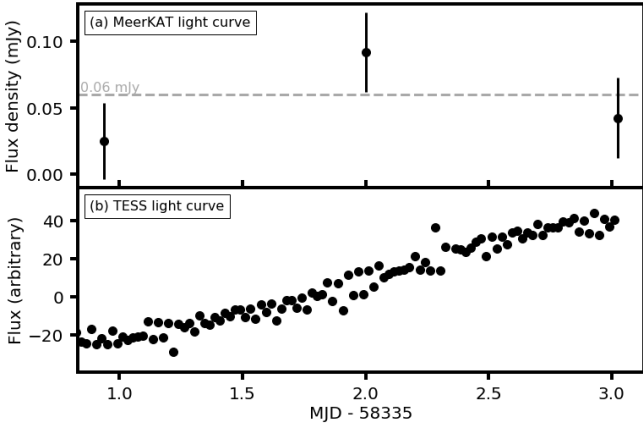


Figure 1. *TESS* and MeerKAT light curves of EXO 0408. The MeerKAT light curve (a) shows the TraP extracted integrated flux density from the full integration images of each epoch. The grey dashed line indicates three times the image RMS noise level. The *TESS* light curve (b) has been cleaned and detrended (see Section 3.3).

	Observation	Flux density (mJy)	S/N
1	2018 August 05 22:26:56.3	0.03 ± 0.03	1.0
2	2018 August 07 00:04:13.7	0.09 ± 0.03	4.5
3	2018 August 08 00:37:04.0	0.04 ± 0.03	2.0

Table 1. The flux density at the position of EXO 0408 in each MeerKAT full time and frequency integration image. The RMS noise of $0.02 \text{ mJy beam}^{-1}$ for each image was used to calculate the S/N.

determined its light curve⁵ using the LOFAR TRANSIENT PIPELINE (TraP, Release 4.0; Swinbank et al. 2015). TraP automatically processes a time series of fits images, detecting sources and extracting light curves. We used the integrated flux density of the source extracted by TraP, where we forced TraP to monitor the position of EXO 0408. This means that we have flux density measurements at that location whether EXO 0408 is detected or not.

The light curve showing the flux density from the full-time-integration images per epoch is shown in Figure 1(a) and the corresponding images are shown in Figure 2. The flux density of EXO 0408 is consistent with zero in the first epoch, the source is detected in the second epoch, and is marginally detected (S/N \sim 2) in the third epoch with a position offset of approximately one pixel ($1''.5$). The flux density of the source in each epoch is shown in Table 1 as well as the signal-to-noise (S/N) in each epoch. Inspection of the shorter-time-integration images revealed no evidence that the source had exhibited a short-duration (<1.5 hr) radio flare and the TraP did not detect the source with a signal-to-noise greater than three in any of the shorter integration images. If we assume the flux density of the source is constant across the three days, the reduced χ^2 value is 1.4, which is not sufficient to reject the null hypothesis that the flux density is constant. As such, we cannot confirm whether the source is constant or variable in the radio at this stage. The source is too faint to determine the in-band radio spectral index using the subband images.

⁵ A light curve is a time series of brightness/flux density measurements for a source.

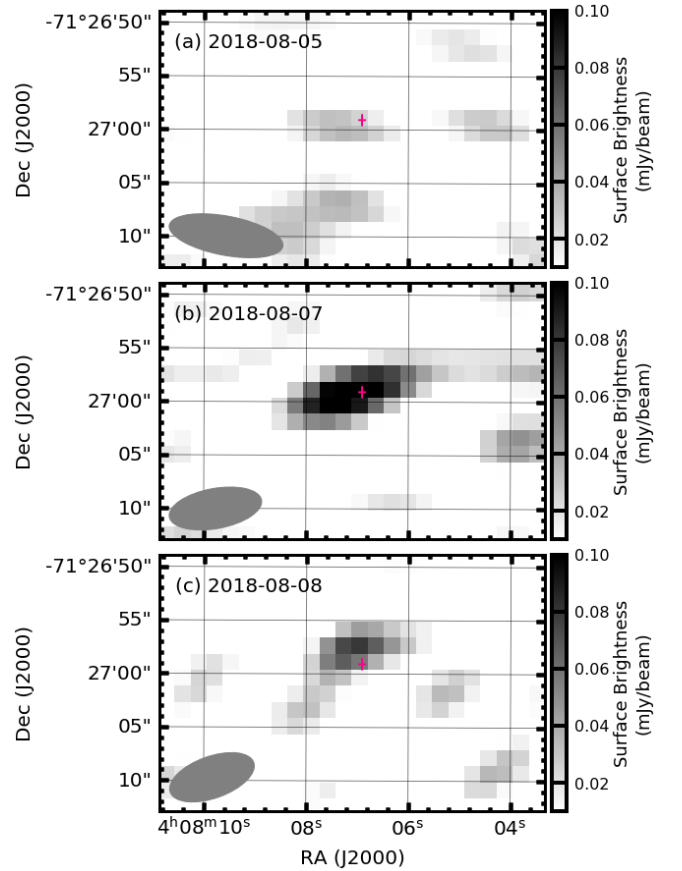


Figure 2. Full time integration MeerKAT images of EXO 0408. The magenta crosshairs show the *Gaia* position. From top to bottom the epochs are: 2018 August 05 22:26:56.3; 2018 August 07 00:04:13.7; and 2018 August 08 00:37:04.0. The synthesised beam shape is shown in the bottom left corner of each panel, and the greyscale is the same in all three images.

2.1 Absolute astrometry

In approximately the first year of observing, there was a known scatter of at worst $3''$ on the astrometry of sources detected by MeerKAT. This issue has since been significantly reduced; however, our observations are from early in the first year of MeerKAT observations. As such, we need to perform astrometric corrections to confirm the positions of sources in the field. To do this, we used the Python Blob Detector and Source Finder (pyBDSF⁶) to determine the positions of sources in the field in each of the three epochs. We used the positions (see Table 2) of four Australian Telescope Compact Array (ATCA) Parkes-MIT-NRAO (PMN) (ATPMN; McConnell et al. 2012) sources in the field of view as reference sources. The median astrometric uncertainty of ATPMN sources is $0''.4$ in both Right Ascension and Declination (McConnell et al. 2012).

We manually confirmed that the ATPMN sources match unresolved MeerKAT sources and solved for an affine transformation matrix to translate and rotate the MeerKAT source positions and applied this transformation to all of the MeerKAT sources. The separation between the MeerKAT and ATPMN reference sources before and after transformation is shown in

⁶ <https://www.astron.nl/citt/pybdsf/>

ATPMN source name	ATPMN RA (deg)	ATPMN Dec (deg)	Epoch 1 separation (″)	Epoch 2 separation (″)	Epoch 3 separation (″)
J040400.5–710908	04 ^h 04 ^m 00 ^s .6	–71°09′08″.9	0.6/0.07	0.7/0.06	0.7/0.07
J040541.4–710449	04 ^h 05 ^m 41 ^s .5	–71°04′49″.8	0.3/0.1	0.4/0.1	0.3/0.1
J040748.6–705712	04 ^h 07 ^m 48 ^s .7	–70°57′12″.5	0.4/0.05	0.4/0.04	0.4/0.05
J040914.4–714205	04 ^h 09 ^m 14 ^s .5	–71°42′05″.3	0.8/0.002	0.5/0.002	0.6/0.002

Table 2. Names and coordinates of the ATPMN reference sources used for absolute astrometry correction and the separation between the ATPMN and MeerKAT reference sources before/after applying the transformation to the source position from each MeerKAT full time and frequency integration image.

Table 2. We performed a Monte Carlo simulation to determine that the uncertainty of the transformation is dominated by the 0[′].4 uncertainty on the ATPMN absolute astrometry.

The *Gaia* EDR3 J2000 proper motion corrected position of EXO 0408 is 04^h08^m07^s.0986 –71°27′00″.852. The uncorrected position of the radio detection on 2018 August 07 00:04:13.7 is 04^h08^m07^s.1±0[′].8 –71°26′59″.3±0[′].8. We then applied the absolute astrometry correction where the change in position of the source due only to the absolute astrometry correction was 0[′].2. We then applied a proper motion correction to the radio position using the *Gaia* proper motion values to find the J2000 position of the source to be: 04^h08^m07^s.1±0[′].9 –71°27′01″.0±0[′].5 where we have added the position uncertainty and the 0[′].4 astrometric uncertainty in quadrature. The separation between the J2000 corrected 2018 August 07 00:04:13.7 radio position and the J2000 corrected *Gaia* position is 0[′].2, which is within the uncertainties on the EXO 0408 radio position. EXO 0408 is the only source identified by Vizier⁷ (Ochsenbein et al. 2000) within 5″ of the corrected radio position.

3 OPTICAL PHOTOMETRY

EXO 0408 has been observed as part of various optical surveys such as *Gaia*, the All-Sky Automated Survey for Supernovae (ASAS-SN; Jayasinghe et al. 2018), and the Deep-Near Infrared Survey of the Southern Sky (DENIS; Cioni et al. 2000).

3.1 Spectral energy distribution

We used archival photometry from Vizier (Ochsenbein et al. 2000) to construct a spectral energy distribution (SED, the full list of references can be found in Appendix A), shown in Figure 3. The BT-SETTL (Allard et al. 2011; Allard 2014) model shown was fit to the SED using the software described in McDonald et al. (2012, 2017) and the *Gaia* DR2 distance of 57.81 ± 0.07 pc was used to scale the luminosity. The model has temperature of 4000 K and a surface gravity (log(*g*) of 4.5). We can see that there is a UV excess, this is likely due to active regions in the stellar atmosphere (e.g. Findeisen et al. 2011).

3.2 Optical variability

EXO 0408 was classified as a rotational variable star by ASAS-SN (Jayasinghe et al. 2018), and a variable star, NSV 15914, by the General Catalogue of Variable Stars (Samus’ et al. 2017). The source was observed 580 times by the All-sky Automated Survey (ASAS;

Pojmanski 1997) from November 2000 to December 2009, by ASAS-SN (Shappee et al. 2014; Kochanek et al. 2017) 345 times in *V*-band from 2017 June to 2018 September, and in *g*-band 2180 times from September 2017 to February 2021. We performed a Lomb-Scargle (Lomb 1976; Scargle 1982; Perera et al. 2018) analysis on the ASAS, ASAS-SN *V*-band, and ASAS-SN *g*-band observations. We did not find a period for the original ASAS observations due to the sparsity of the data points. Both the ASAS-SN *V*- and *g*-band observations are affected by the approximately daily observing cadence; however, we find a period of 5.13 ± 0.03 days for the ASAS-SN *V*-band observations, and a period of 5.20 ± 0.02 days for the ASAS-SN *g*-band observations. These are consistent with the 5.2 ± 0.20 day period found by Cutispoto et al. (1996). The median *V*-band magnitude is 12.4 mag from both ASAS and ASAS-SN, and the median ASAS-SN *g*-band magnitude is 13.1 mag.

3.3 TESS optical photometry

EXO 0408 has been observed in 13 Transiting Exoplanet Survey Satellite (*TESS*; Ricker et al. 2015) sectors. *TESS* first observed the source in July 2018 and the last observations were taken in July 2019. Günther et al. (2020) found 11 flares from EXO 0408 in an automated search for stellar flares from M-dwarfs in the first 2 *TESS* sectors. We can see in Figure 1 that there is no optical flare during the MeerKAT observations. From the *TESS* observations, Günther et al. (2020) also found a rotational period of 4.92 days (no uncertainty is given), which is broadly consistent with the 5.2 ± 0.20 day period.

The *TESS* Input Catalogue (TIC) Identifier for EXO 0408 is 25132999. Upon inspection of the *TESS* images, there is a nearby source with coordinates 04^h07^m56^s.190 –71°26′36″.851 and TIC 25132995 that is partially blended with EXO 0408. We extracted *TESS* light curves for this source as well as EXO 0408 and another nearby source, TIC 677356964 with coordinates 04^h08^m44^s.444 –71°28′49″.696. We extracted the light curve for TIC 25132995 to determine whether the periodicity found for EXO 0408 has been affected or induced by this source. We extracted the light curve for TIC 677356964 to find and eliminate systematic problems with the light curves. We removed any part of the light curve where at least two of the three sources have correlated systematic issues, and removed two sectors where the data were strongly affected by systematics. We then divided each sector into parts where there was a gap in observations of two days or more, and for each part we removed any linear trend in the data. We performed a Lomb-Scargle analysis on all of the clean, de-trended data and found a period of 5.18±0.04 days. The Lomb-Scargle periodogram is shown in Figure 4. When we fold the data to 5.18 days, shown in Figure 5, we find that the shape of the curve and phase of the peak is consistent across the year of *TESS* observations. Due to the challenge of calibrating the absolute flux of *TESS* observations, the amplitude of the observations shown here are arbitrary and not scaled relative to

⁷ <http://vizier.cfa.harvard.edu/viz-bin/VizieR>

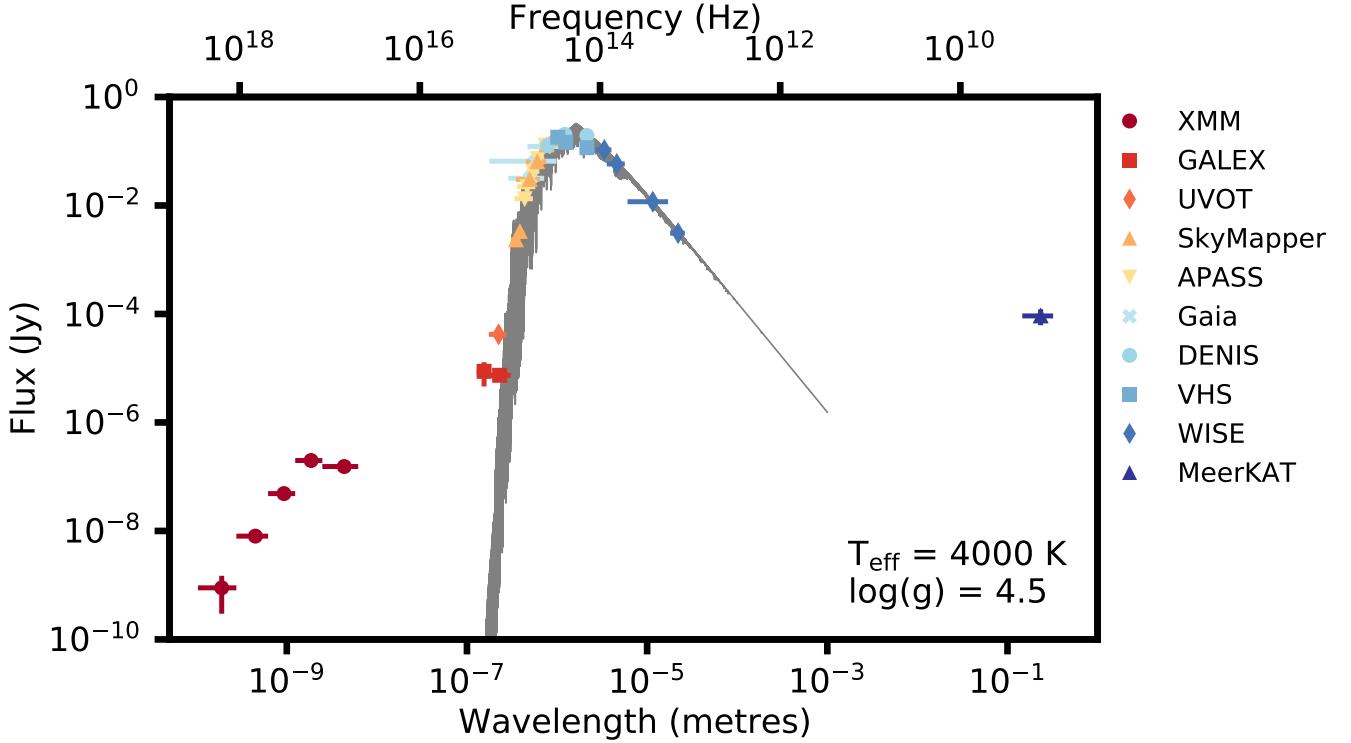


Figure 3. SED of EXO 0408 using the literature data points (see Appendix A), including the MeerKAT detection and the X-ray detections in Table 3. The grey line is the BT-SETTL model fit to the data points, with $T_{\text{eff}} = 4000$ K, $\log_{10}(g) = 4.5$, $[\text{Fe}/\text{H}] = 0$ and $[\alpha/\text{Fe}] = 0$.

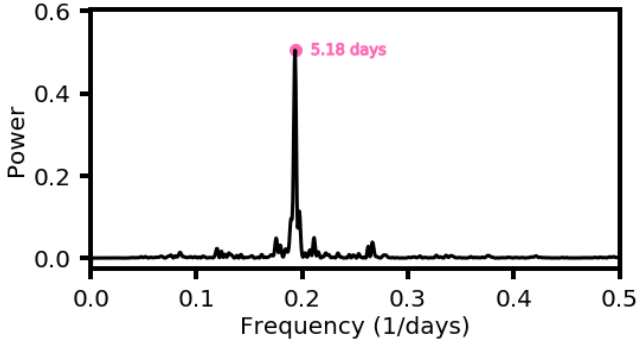


Figure 4. TESS Lomb-Scargle periodogram generated using the clean, detrended data. The 5.18 day period is indicated.

each sector. We have not verified the nature of the bright, short bursts.

4 OPTICAL SPECTROSCOPY

We observed EXO 0408 with the Southern African Large Telescope (SALT; Buckley et al. 2006) High Resolution Spectrograph (HRS; Bramall et al. 2012; Crause et al. 2014) on 2021 February 17.7835 in clear conditions and $\sim 1''$ seeing. SALT is located at the South African Astronomical Observatory (SAAO) site in Sutherland, South Africa, and HRS is a fibre-fed, dual-beam, white-pupil, vacuum-stabilised, high-resolution ($R = 13,000\text{--}74,000$, depending on mode and wavelength) spectrograph. The HRS spectrum was

taken in low-resolution mode with an integration time of 1200 seconds. Blue (3800–5550Å) and red (5450–8900Å) spectra were obtained at average resolutions of 0.3Å and 0.5Å, respectively, and were calibrated using the weekly set of HRS calibrations, including ThAr arc spectra and QTH lamp flat-fields. Two identical fibres sampled the object and a nearby (20 arcsec) sky region, producing interleaving échelle orders, which were reduced using the SALT HRS MIDAS pipeline (Kniazev et al. 2016) to produce a sky subtracted spectrum, a sample of which is shown in Figure 6.

The spectrum confirms that the source is a chromospherically active M-dwarf with a temperature of 4000 ± 200 K. The chromospheric activity is identified using the H α line, which is in emission with a filled core (see Figure 6(c)) and the calcium H & K lines and near-infrared calcium triplet, which are in absorption with strong core emission (see Figure 6(a) and (e)). In Figure 6(d) we can see that there is no lithium absorption and we do not see any lines suggesting a binary companion.

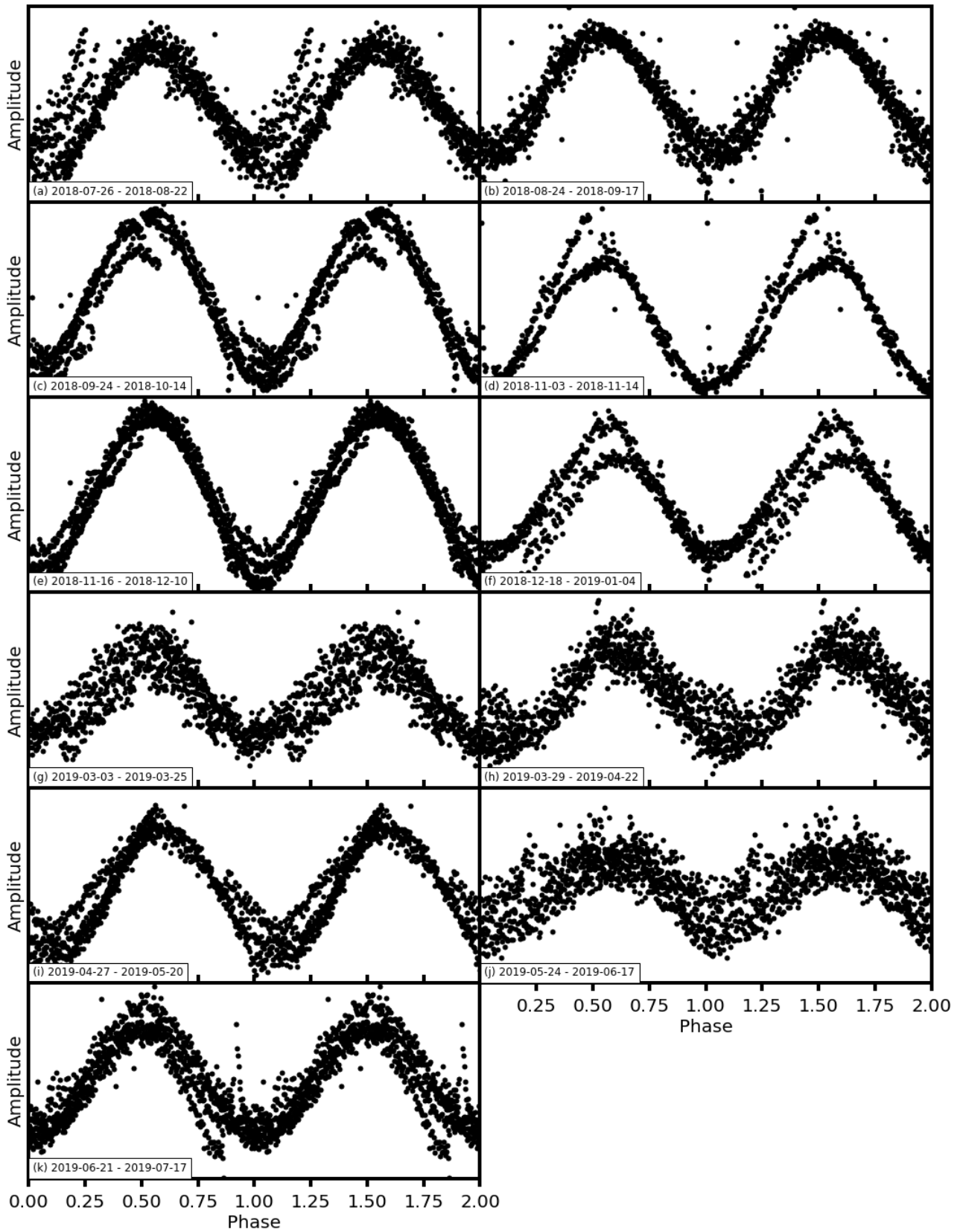


Figure 5. Eleven *TESS* sectors folded to a period of 5.18 ± 0.04 days, 2 sectors were not included due to data issues. Note that the amplitude is arbitrary and we have not verified the short, bright bursts as real flares.

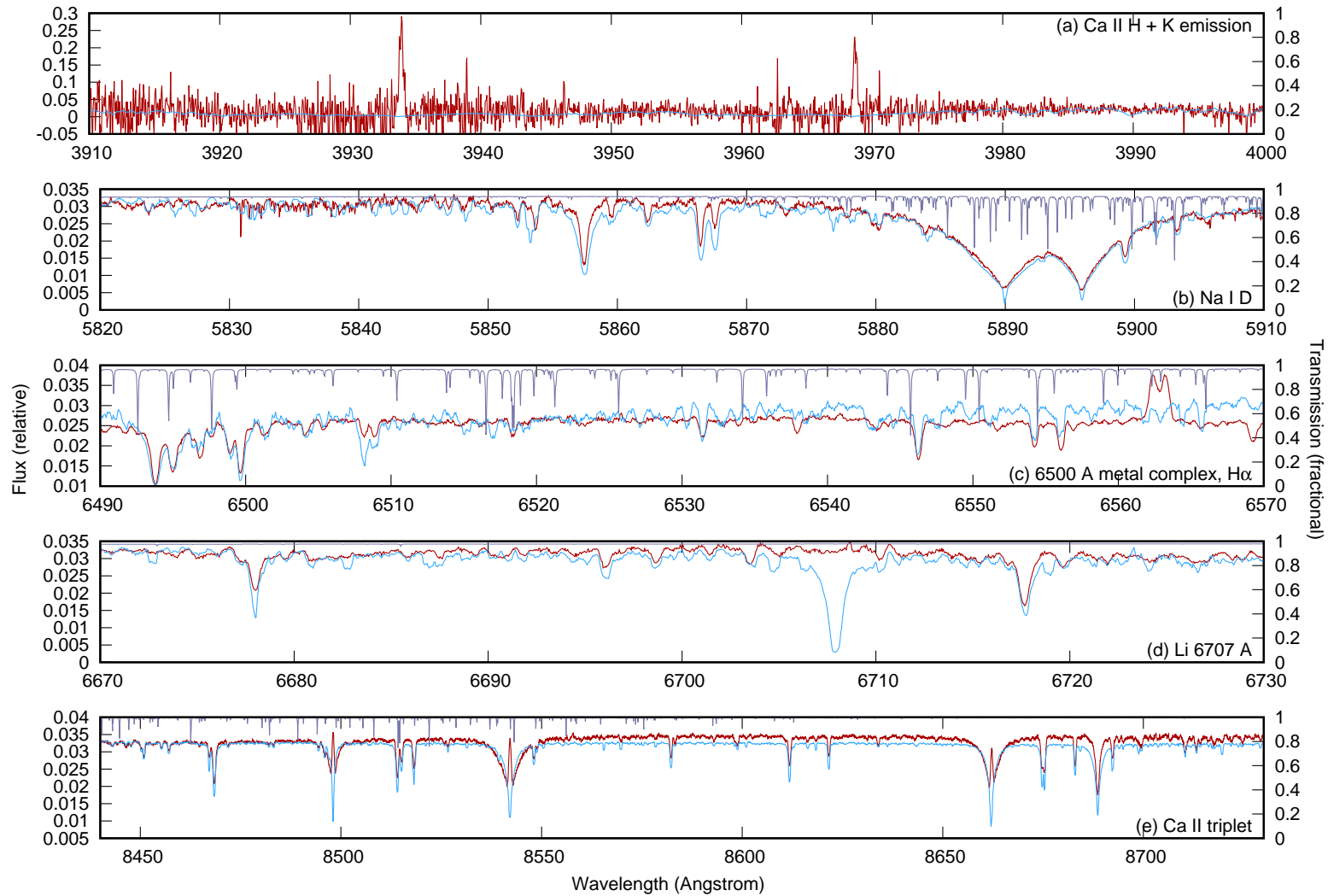


Figure 6. SALT HRS spectrum of EXO 0408. The red lines are the spectrum of EXO 0408, the cyan lines are the same model spectrum used in Figure 3, and the purple lines show the atmospheric transmission. The spectrum has been corrected for a radial velocity of 16 km s^{-1} . Panel (a) shows the Ca II H & K lines, panel (b) shows the Na I D lines, panel (c) shows the 6500 Å metal line complex and H α (double-peaked emission line), panel (d) shows the Li 6707 Å line, and panel (e) shows the Ca II triplet.

Band (keV)	Flux (mW m ⁻²)	Luminosity (erg s ⁻¹)
0.2-0.5	$(1.1170 \pm 0.0371) \times 10^{-13}$	$(4.5 \pm 0.1) \times 10^{28}$
0.5-1.0	$(2.4021 \pm 0.0547) \times 10^{-13}$	$(9.6 \pm 0.2) \times 10^{28}$
1.0-2.0	$(1.1804 \pm 0.0417) \times 10^{-13}$	$(4.7 \pm 0.2) \times 10^{28}$
2.0-4.5	$(0.4850 \pm 0.0493) \times 10^{-13}$	$(1.9 \pm 0.2) \times 10^{28}$
4.5-12	$(0.1620 \pm 0.108) \times 10^{-13}$	$(0.6 \pm 0.4) \times 10^{28}$
0.2-12	$(5.4914 \pm 0.152) \times 10^{-13}$	$(22.0 \pm 0.6) \times 10^{28}$
0.5-4.5	$(5.2819 \pm 0.102) \times 10^{-13}$	$(21.1 \pm 0.4) \times 10^{28}$

Table 3. *XMM-Newton* bands and fluxes for EXO 0408.

5 X-RAY AND UV OBSERVATIONS

As well as the original *EXOSAT* observations, EXO 0408 has been observed by *XMM-Newton* and *ROSAT*. The source was faintly detected in the *ROSAT* All-Sky-Survey (Voges et al. 1999) and was detected once serendipitously in the *XMM-Newton* slew survey on 2011 September 22 (XMM-SSC 2018). The mean flux and luminosity in each *XMM-Newton* band is shown in Table 3.

VWHyi was monitored by *Swift* as part of the ThunderKAT observations; however, EXO 0408 did not fall into the FoV of the X-ray Telescope (*Swift* XRT). EXO 0408 did fall within the Ultraviolet/Optical Telescope (UVOT; Mason et al. 2000) FoV during these observations, on 2018 July 31 while observing with the UM2 filter (centred on 2246 Å) and it was detected with an AB magnitude of 19.84 ± 0.21 . EXO 0408 has also been detected in Galaxy Evolution Explorer Data Release 5 (GALEX-DR5; Bianchi et al. 2011), with FUV (1344-1786 Å) and NUV (1771-2831 Å) AB magnitudes of 21.544 and 20.176 respectively.

6 DISCUSSION

EXO 0408 is the first radio M-dwarf detected with MeerKAT. We have placed the source on the Güdel plot (Figure 7, the Güdel–Benz relation, shown as a dashed line) using the *EXOSAT* quiescent X-ray flux, adjusted for the new 57.81 pc distance. We can see that the more recent *XMM-Newton* X-ray luminosities (Table 3) are consistent with the *EXOSAT* luminosity. The blue upper limit assumes that the detection in the second MeerKAT epoch is a flare, and uses the non-detection upper limit on the radio flux density from the full-time-integration image of the first epoch. The orange marker assumes that the detection in the second epoch is the quiescent radio flux density of the source. These are only estimates of the position of the source on the plot, as the quiescent radio and X-ray emission should ideally be measured simultaneously. We can see that in both cases EXO 0408 fits well with the relation and with the M-dwarfs in the plot.

We can determine limits on the brightness temperature, T_b , of the radio detection of EXO 0408 using the formula:

$$T_b = \frac{c^2}{\kappa \nu^2} \cdot F_\nu \cdot \frac{d^2}{A^2} \quad (1)$$

(Dulk 1985) where c is the speed of light, κ is the Boltzmann constant, ν is the observing frequency, F_ν is the flux density at frequency ν , d is the distance to the source, and A is the projected area of the emitting region where $A = \pi R_*^2$. If we assume a typical M-dwarf stellar radius of $0.6 M_\odot$ and that the emitting radio region is twice the radius of the star, then $A = 1.5 \times 10^{22}$ cm. Using the MeerKAT 1284 MHz flux density of the EXO 0408 when it was detected on 2018 August 07 (0.09 ± 0.03 mJy) we find the corresponding brightness temperature to be $T_b \sim 2 \times 10^9$ K, which

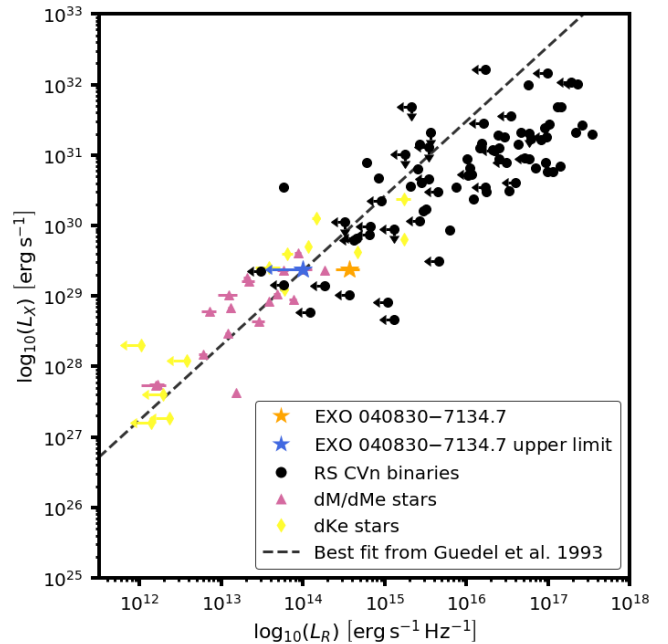


Figure 7. Radio specific quiescent luminosities and X-ray quiescent luminosities of stars (Güdel plot) showing the sources from Guedel & Benz (1993) and EXO 0408. The blue EXO 0408 upper limit is the radio upper limit from the first epoch, which assumes that the detection in the second epoch is a flare. The orange EXO 0408 point is the flux density in the second epoch, which assumes the detection is the quiescent radio emission from the source. The Güdel–Benz relation is shown using a dashed-line.

is consistent with an incoherent emission mechanism. This is likely a lower limit on the brightness temperature, as we are assuming a large emitting region. If we assume instead a plasma loop with radius $\sim 7 \times 10^8$ cm (Stepanov et al. 2001), the brightness temperature could reach $T_b \sim 2 \times 10^{13}$ K, which would imply a coherent emission mechanism. Polarisation information and a radio spectrum would assist in determining the type radio emission; however, the polarisation properties of MeerKAT images away from the phase centre are still being categorised and data processing methods developed. As such, polarisation studies of this source will be investigated as part of future work. The source is insufficiently bright to measure the radio spectrum or to determine any meaningful constraints. The estimated brightness temperature of EXO 0408 (assuming a large emission region), the position on the Güdel–Benz plot (Figure 7) and the chromospheric activity indicated by the H α , calcium H & K lines, and near-infrared calcium triplet suggest that the radio emission is incoherent gyrosynchrotron emission.

The SED, optical spectrum, and photometric variability support the conclusion that EXO 0408 is a magnetically active, rotating, single M-dwarf and that the radio emission that we observed with MeerKAT is either an incoherent flare or quiescent emission. We used *TESS* photometry to reveal that the rotational period of EXO 0408 is 5.18 ± 0.04 days, and to show that there is no optical flare at the time of the radio observations. Simultaneous optical and radio monitoring of Proxima Centauri by Zic et al. (2020) detected an optical flare a few hours before the detection of a radio flare and they found that the optical and radio emission were from a Type IV burst linked to a coronal mass ejection. However; optical and radio

bursts are not necessarily observed together and can be produced by different flaring mechanisms.

EXO 0408 is only the first MeerKAT detection of a radio star, but we can use recent searches for stellar radio emission to determine whether this detection is consistent with the expected rates. The FWHM of MeerKAT is $\sim 1 \text{ deg}^{-2}$, we therefore have a surface density of radio detected M-dwarfs of 1 deg^{-2} at 1284 MHz with a sensitivity of $0.03 \text{ mJy beam}^{-1}$. Pritchard et al. (2021) searched ASKAP Stokes I and V images at 887.5 MHz and found radio emission from 33 stars, 23 of which had no previous radio detections. They determine that the surface density of radio loud cool dwarfs stars at 887.5 MHz is $5.27^{+3.06}_{-2.15} \times 10^{-4} \text{ deg}^{-2}$ with a sensitivity of $0.25 \text{ mJy beam}^{-1}$. Using the same scaling relation as Pritchard et al. (2021) ($N(> S) \propto S^{-3/2}$ where N is the number of stars and S is the flux density) the ASKAP result scales to 0.01 deg^{-2} for MeerKAT. Using the Faint Images of the Radio Sky at Twenty Centimetres (FIRST; Becker et al. 1995) survey Helfand et al. (1999) searched $\sim 5000 \text{ deg}^2$ with a sensitivity of $0.07 \text{ mJy beam}^{-1}$ at 1400 MHz and found 26 stellar radio sources. This corresponds to a surface density of $5.2 \times 10^{-3} \text{ deg}^{-2}$, which scales to 0.6 deg^{-2} using the sensitivity of the MeerKAT observations of EXO 0408. As we search more MeerKAT observations for stellar sources our statistics will become more robust, but using this one source our rate is more consistent with the FIRST rate than the ASKAP rate. This could be because cool dwarfs are more active at $\sim 1400 \text{ MHz}$ than at $\sim 900 \text{ MHz}$, or it could be due to the different search methods. We searched for radio emission at the position of a known active star and Helfand et al. (1999) matched the position of radio sources to the known positions of stars. Whereas Pritchard et al. (2021) searched specifically for circularly polarised searches. This may mean that they are missing radio stars with circular polarisation fractions below their threshold. The MeerKAT Galactic Plane Survey will be particularly interesting for investigating the distribution and surface density of stellar radio sources (Thompson et al. 2016).

7 CONCLUSIONS

We observe radio emission from the known X-ray flaring star EXO 0408 during MeerKAT observations of the CV VW H γ . We use the SED and new SALT spectroscopy of the source to confirm that it is an M-dwarf, with a temperature of $4000 \pm 200 \text{ K}$ and spectral emission lines indicating chromospheric activity. We use *TESS* optical photometry to determine that the rotational period of the star is 5.18 ± 0.04 days. This is the first radio emission detected from the star, and the first MeerKAT detection of an M-dwarf flare star. The radio brightness temperature, the X-ray and radio luminosity, and the chromospheric activity of the star indicate that the radio emission is incoherent gyrosynchrotron radiation. This detection shows the importance of commensal searches for variable and transient radio sources, and their potential for finding more radio stars.

ACKNOWLEDGEMENTS

LND and BWS acknowledge support from the European Research Council (ERC) under the European Union’s Horizon 2020 research and innovation programme (grant agreement No 694745). DRAW was supported by the Oxford Centre for Astrophysical Surveys, which is funded through generous support from the Hintze Family

Charitable Foundation. DAHB acknowledges research support from the South African National Research Foundation. We acknowledge use of the Inter-University Institute for Data Intensive Astronomy (IDIA) data intensive research cloud for data processing. IDIA is a South African university partnership involving the University of Cape Town, the University of Pretoria and the University of the Western Cape. The MeerKAT telescope is operated by the South African Radio Astronomy Observatory (SARAO), which is a facility of the National Research Foundation, an agency of the Department of Science and Technology. We would like to thank the operators, SARAO staff and ThunderKAT Large Survey Project team. The Parkes radio telescope is part of the Australia Telescope National Facility which is funded by the Commonwealth of Australia for operation as a National Facility managed by CSIRO. Some of these observations were obtained with the Southern African Large Telescope under the Large Science Programme on transients, 2018-2-LSP-001 (PI: DAHB). This work has made use of data from the European Space Agency (ESA) mission *Gaia*.⁸ Funding for the DPAC has been provided by national institutions, in particular the institutions participating in the *Gaia* Multilateral Agreement. This research made use of Astropy,⁹ a community-developed core Python package for Astronomy (Astropy Collaboration et al. 2013; Price-Whelan et al. 2018). This research made use of APLpy, an open-source plotting package for Python (Robitaille & Bressert 2012).

DATA AVAILABILITY

The data underlying this article are available in Zenodo at <https://doi.org/10.5281/zenodo.5084298>. The code underlying this article is available on GitHub and Zenodo: <https://github.com/ianHeywood/oxkat>, <https://doi.org/10.5281/zenodo.4515114>, <https://doi.org/10.5281/zenodo.4456303> and <https://doi.org/10.5281/zenodo.4921715>.

REFERENCES

- Allard F., 2014, in Booth M., Matthews B. C., Graham J. R., eds, Vol. 299, *Exploring the Formation and Evolution of Planetary Systems*. pp 271–272, doi:10.1017/S1743921313008545
- Allard F., Homeier D., Freytag B., 2011, in Johns-Krull C., Browning M. K., West A. A., eds, *Astronomical Society of the Pacific Conference Series* Vol. 448, 16th Cambridge Workshop on Cool Stars, Stellar Systems, and the Sun. p. 91 (arXiv:1011.5405)
- Astropy Collaboration et al., 2013, *A&A*, **558**, A33
- Bailer-Jones C. A. L., Rybizki J., Fousneau M., Demleitner M., Andrae R., 2021, *AJ*, **161**, 147
- Bastian T. S., 1990, *Sol. Phys.*, **130**, 265
- Becker R. H., White R. L., Helfand D. J., 1995, *ApJ*, **450**, 559
- Benz A. O., Guedel M., 1994, *Astronomy & Astrophysics*, **285**, 621
- Bianchi L., Herald J., Efremova B., Girardi L., Zabot A., Marigo P., Conti A., Shiao B., 2011, *Ap&SS*, **335**, 161
- Bramall D. G., et al., 2012, in *Ground-based and Airborne Instrumentation for Astronomy IV*. p. 84460A, doi:10.1117/12.925935

⁸ <https://www.cosmos.esa.int/gaia>, processed by the *Gaia* Data Processing and Analysis Consortium (DPAC, <https://www.cosmos.esa.int/web/gaia/dpac/consortium>)

⁹ <http://www.astropy.org>

- Buckley D. A. H., Swart G. P., Meiring J. G., 2006, in Society of Photo-Optical Instrumentation Engineers (SPIE) Conference Series. p. 62670Z, doi:10.1117/12.673750
- Callingham J. R., et al., 2021, *Nature Astronomy*,
- Camilo F., et al., 2018, *ApJ*, **856**, 180
- Cioni M. R., et al., 2000, *A&AS*, **144**, 235
- Crause L. A., et al., 2014, in Ground-based and Airborne Instrumentation for Astronomy V. p. 91476T, doi:10.1117/12.2055635
- Cutispoto G., Tagliaferri G., Pallavicini R., Pasquini L., Rodono M., 1996, *A&AS*, **115**, 41
- Cutri R. M., et al. 2012, VizieR Online Data Catalog, p. II/311
- Drake A. J., et al., 2009, *ApJ*, **696**, 870
- Dressing C. D., Charbonneau D., 2015, *ApJ*, **807**, 45
- Driessen L. N., et al., 2020, *MNRAS*, **491**, 560
- Dufour P., Blouin S., Coutu S., Fortin-Archambault M., Thibeault C., Bergeron P., Fontaine G., 2017, in Tremblay P. E., Gaensicke B., Marsh T., eds, *Astronomical Society of the Pacific Conference Series Vol. 509*, 20th European White Dwarf Workshop. p. 3 (arXiv:1610.00986)
- Dulk G. A., 1985, *ARA&A*, **23**, 169
- Fender R., et al., 2017, arXiv e-prints, p. arXiv:1711.04132
- Findeisen K., Hillenbrand L., Soderblom D., 2011, *AJ*, **142**, 23
- Forbrich J., et al., 2011, in Johns-Krull C., Browning M. K., West A. A., eds, *Astronomical Society of the Pacific Conference Series Vol. 448*, 16th Cambridge Workshop on Cool Stars, Stellar Systems, and the Sun. p. 455 (arXiv:1012.1626)
- Gaia Collaboration 2020a, VizieR Online Data Catalog, p. I/350
- Gaia Collaboration 2020b, VizieR Online Data Catalog, p. I/350
- Gaia Collaboration et al., 2018, *A&A*, **616**, A1
- Guedel M., Benz A. O., 1993, *ApJ*, **405**, L63
- Günther M. N., et al., 2020, *AJ*, **159**, 60
- Hardegree-Ullman K. K., Cushing M. C., Muirhead P. S., Christiansen J. L., 2019, *AJ*, **158**, 75
- Helfand D. J., Schnee S., Becker R. H., White R. L., McMahon R. G., 1999, *AJ*, **117**, 1568
- Henden A. A., Levine S., Terrell D., Welch D. L., 2015, in *American Astronomical Society Meeting Abstracts #225*. p. 336.16
- Heywood I., 2020, oxxat: Semi-automated imaging of MeerKAT observations (ascl:2009.003)
- Hotan A. W., et al., 2021, *Publ. Astron. Soc. Australia*, **38**, e009
- Jayasinghe T., et al., 2018, *MNRAS*, **477**, 3145
- Kenyon J. S., Smirnov O. M., Grobler T. L., Perkins S. J., 2018, *MNRAS*, **478**, 2399
- Kepler S. O., et al., 2013, *MNRAS*, **429**, 2934
- Kniazev A. Y., Gvaramadze V. V., Berdnikov L. N., 2016, *MNRAS*, **459**, 3068
- Kochanek C. S., et al., 2017, *PASP*, **129**, 104502
- Kurtzer G. M., Sochat V., Bauer M. W., 2017, *PLoS one*, **12**, e0177459
- Lépine S., Gaidos E., 2011, *AJ*, **142**, 138
- Lomb N. R., 1976, *Ap&SS*, **39**, 447
- Makhathini S., 2018, PhD thesis, Rhodes University, Drosty Rd, Grahamstown, 6139, Eastern Cape, South Africa
- Mason K. O., Cropper M. S., Kennedy T. E., Nousek J., Roming P., McLelland M., 2000, in *AAS/High Energy Astrophysics Division #5*. p. 34.11
- Matthews L. D., 2019, *Publications of the ASP*, **131**, 016001
- McConnell D., Sadler E. M., Murphy T., Ekers R. D., 2012, *MNRAS*, **422**, 1527
- McDonald I., Zijlstra A. A., Boyer M. L., 2012, *MNRAS*, **427**, 343
- McDonald I., Zijlstra A. A., Watson R. A., 2017, *MNRAS*, **471**, 770
- McMahon R. G., Banerji M., Gonzalez E., Koposov S. E., Bejar V. J., Lodieu N., Rebolo R., VHS Collaboration 2013, *The Messenger*, **154**, 35
- McMullin J. P., Waters B., Schiebel D., Young W., Golap K., 2007, in Shaw R. A., Hill F., Bell D. J., eds, *Astronomical Society of the Pacific Conference Series Vol. 376*, *Astronomical Data Analysis Software and Systems XVI*. p. 127
- Ochsenbein F., Bauer P., Marcout J., 2000, *A&AS*, **143**, 23
- Offringa A. R., McKinley B., Hurley-Walker et al., 2014a, *MNRAS*, **444**, 606
- Offringa A. R., McKinley B., Hurley-Walker et al., 2014b, *MNRAS*, **444**, 606
- Perera B. B. P., et al., 2018, *MNRAS*, **478**, 218
- Pojmanski G., 1997, *Acta Astron.*, **47**, 467
- Price-Whelan A. M., et al., 2018, *AJ*, **156**, 123
- Pritchard J., et al., 2021, *MNRAS*, **502**, 5438
- Ricker G. R., et al., 2015, *Journal of Astronomical Telescopes, Instruments, and Systems*, **1**, 014003
- Robitaille T., Bressert E., 2012, APLpy: Astronomical Plotting Library in Python, *Astrophysics Source Code Library (ascl:1208.017)*
- Samus' N. N., Kazarovets E. V., Durlevich O. V., Kireeva N. N., Pastukhova E. N., 2017, *Astronomy Reports*, **61**, 80
- Scargle J. D., 1982, *ApJ*, **263**, 835
- Shappee B. J., et al., 2014, *ApJ*, **788**, 48
- Stepanov A. V., Kliem B., Zaitsev V. V., Fürst E., Jessner A., Krüger A., Hildebrandt J., Schmitt J. H. M. M., 2001, *A&A*, **374**, 1072
- Swinbank J. D., et al., 2015, *Astronomy and Computing*, **11**, 25
- Thompson M., et al., 2016, in *MeerKAT Science: On the Pathway to the SKA*. p. 15
- Vedantham H. K., et al., 2020, *Nature Astronomy*, **4**, 577
- Villadsen J. R., 2017, PhD thesis, California Institute of Technology
- Villadsen J., Hallinan G., 2019, *The Astrophysical Journal*, **871**, 214
- Voges W., et al., 1999, *A&A*, **349**, 389
- Wenger M., et al., 2000, *Astronomy and Astrophysics Supplement Series*, **143**, 9
- White N. E., Peacock A., 1988, *Mem. Soc. Astron. Italiana*, **59**, 7
- Wolf C., et al., 2018, *Publ. Astron. Soc. Australia*, **35**, e010
- XMM-SSC 2018, VizieR Online Data Catalog, p. IX/53
- Zic A., et al., 2020, *ApJ*, **905**, 23
- van der Woerd H., Tagliaferri G., Thomas H. C., Beuermann K., 1989, *A&A*, **220**, 221

APPENDIX A: SUPPLEMENTARY MATERIAL

The sources for the optical SED shown in Figure 3 are:

- *Gaia* Data Release 2. Summary of the contents and survey properties ([Gaia Collaboration et al. 2018](#))
- VizieR Online Data Catalog: *Gaia* Early Data Release 3 (EDR3; [Gaia Collaboration 2020b](#))
- VizieR Online Data Catalog: Wide-field Infrared Survey Explorer (WISE) All-Sky Data Release ([Cutri & et al. 2012](#))
- Galaxy Evolution Explorer (GALEX) catalogs of UV sources: statistical properties and sample science applications: hot white dwarfs in the Milky Way ([Bianchi et al. 2011](#))
- American Association of Variable Star Observers (AAVSO) Photometric All-Sky Survey (APASS) - The Latest Data Release ([Henden et al. 2015](#))
- SkyMapper Southern Survey: First Data Release ([Wolf et al. 2018](#))
- The Deep-Near Infrared Survey of the Southern Sky (DENIS; [Cioni et al. 2000](#))
- The Visible and Infrared Survey Telescope for Astronomy (VISTA) Hemisphere Survey (VHS; [McMahon et al. 2013](#))

This paper has been typeset from a $\text{\TeX}/\text{\LaTeX}$ file prepared by the author.